Stochastic ice accretion model using an unstructured advancing front technique

Helene Papillon Laroche, Emmanuel Radenac, Eric Laurendeau

Stochastic Ice Accretion Model Using an Unstructured Advancing Front Technique

Helene Papillon Laroche[a,*], Emmanuel Radenac[b], Eric Laurendeau[a]

[a] *Polytechnique Montreal, Montreal, Canada*
[b] *ONERA/DMPE, Université de Toulouse, F-31055 Toulouse, France*

Abstract

This paper describes a stochastic ice accretion method to model in-flight ice accretion. The approach consists in complementing the deterministic quasi-steady process generally used to simulate ice accretion by treating the effects of water-droplet deposition and freezing on the ice growth in a stochastic and unsteady manner. The baseline algorithm thus features an unstructured advancing front technique modeling the freezing of individual water particles. Stochasticity is introduced in the seeding process by generating a random initial position and diameter for each injected particle. The particles are treated sequentially and their impingement position is obtained from their trajectory, which is extracted as a streamline of the deterministic quasi-steady droplet velocity field computed by an Eulerian droplet impingement model. The thermodynamic state of the deposited water is then assessed and an advancing front algorithm is used to generate the corresponding elements of ice, which allows capturing the unsteady behavior of the ice growth. The mass of water to be frozen is given by the freezing fraction, computed by the deterministic quasi-steady approach, the remaining mass flowing downstream until the particle is completely frozen. Unlike deterministic approaches, the process treats the ice density as a dependent variable. The verification of the model shows its convergence according to the ice element size, which is the main computational parameter.

*Corresponding author
Email address: helene.papillon-laroche@polymtl.ca (Helene Papillon Laroche)

An extended 2D model is presented to cater for 3D effects by introducing the concept of permeability of the ice front. Validation is performed by comparing the obtained ice shapes to the experimental results for four test cases of the literature. The method successfully captures both rime and glaze ice geometries. Finally, the stochasticity observed in the experimental ice shapes and the formation of discrete ice structures are well captured, which are usually missed by the state-of-the-art deterministic icing frameworks.

Keywords: In-flight icing, Ice accretion model, Modeling, Stochasticity, Non-deterministic

1. Introduction

In-flight icing is primarily due to the impingement of supercooled water droplets on the exposed surface of an aircraft (Trontin and Villedieu, 2018). As the ice accumulates, it leads to changes in the aircraft geometry, which may result in aerodynamic performance degradation. Even though it is a well-known hazard, the extent of the underlying mechanisms involved is not yet fully understood. Computational models are developed to better assess the impact of such phenomena.

State-of-the-art icing software mainly implement a deterministic and continuous framework in which the mathematical foundations are based on partial differential equations, as presented at the first Ice Prediction Workshop (IPW) (Laurendeau et al., 2022). For such solvers, the calculation procedure is sequential and quasi-steady. The aerodynamic flow is first solved around the clean surface. The droplet trajectories are then computed. The freezing and runback of the deposited water are finally simulated. These physical models are solved in the steady state because the ice growth has a very long characteristic time and the flow is thus considered as established around a fixed shape.

As the ice grows, the shape of the exposed surface is updated with a user-specified time-step. Multi-stepping can be used: the quasi-steady process is looped several times. The number of loops (i.e., steps) is usually the result of a

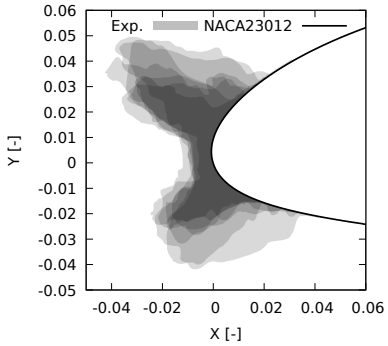

Figure 1: Experimental variability of the ice shape - IPW's Case 242 (Oztekin, 2021; Broeren, 2021). The grayscale represents the likelihood of the results : the darker the area is, the most probable it is the obtained ice at this position

trade-off between computation time, accuracy and empirical know-how.

In such frameworks, the final ice shape is smooth, continuous and corresponds to a converged solution of the systems of equations. However, in real icing conditions, the obtained experimental shapes are variable, as presented in Figure 1, where seven different experimental ice shapes are represented for the same icing tunnel conditions (Case 242 (Lee et al., 2014; Laurendeau et al., 2022), described in table 1). One can observe significant variations within the ice shapes, which are missed by the state-of-the-art icing frameworks. This can lead to inaccurate predictions of the ice shapes and thus, the associated performance degradations.

Previous works proposed non-deterministic frameworks to reproduce the observed stochasticity in the experimental ice shapes. Szilder originally developed the Morphogenetic Model (Szilder and Lozowski, 2004), a particle-based method that discretizes the accretion domain with a complete Cartesian grid. The cells of this lattice are filled by individual particles of water according to the impingement and freezing processes. Following the impingement of a particle, the runback water is modeled by a random walk: the particle moves downstream, from cell to cell, and freezes according to the results of a comparison

between a random number and a probability of freezing (Forsyth and Szilder, 2022). The latter is computed according to the icing conditions. Butnarasu *et al.* proposed a multi-layer extension of the Morphogenetic model using the software FENSAP-ICE (Butnarasu et al., 2015). While the approach and its extension successfully model complex and variable ice shapes, the use of a complete Cartesian grid represents a drawback as the associated computational cost is significant. Bourgault-Côté re-examined the Morphogenetic approach by proposing a Cartesian advancing front technique to reduce the computational cost in a multi-layer framework using B-splines to re-generate a valid and continuous geometry from the discrete ice shape after each layer (Bourgault-Côté, 2019; Papillon-Laroche et al., 2021). Stochasticity is introduced in both the impingement and freezing process through the use of probabilities. The stochastic impingement is controlled by the collection efficiency obtained from an Eulerian droplet solver converted directly to an impingement probability. One drawback of this approach is its inability to predict glaze ice shape, as stated in the works of Bourgault-Côté (2019) and Papillon-Laroche et al. (2021). Other works, such as Leroy (2004) and Yuki and Yamamoto (2014), proposed meshless approaches to model the discontinuous and random growth of the ice. Their models discretize the fluid elements using either individual spheres of ice or clusters of small particles. The main source of stochasticity in both methods comes from the seeding of the droplets in the accretion domain. It is interesting to note that all these approaches revisit the assumption of pure quasi-stationarity of droplet deposition with respect to the evolution of the exposed surface. The two physics are linked in these methods by updating the ice shape exposed to droplet deposition and taking into account the potential effects of the ice shape on the droplet deposition.

This paper proposes a complete two-dimensional (2D) ice accretion model using an unstructured advancing front technique to model the phenomenon in a building block manner, following the work of Papillon-Laroche (2022). It features a stochastic impingement process based on the extraction of the droplet trajectories. The prediction of complex ice morphologies is enabled by a com-

plete freezing process and a finer coupling between the geometry evolution and the droplet trajectories, despite the proposed method being a single-layer framework (i.e. the field values are computed only once at the beginning of the process). This paper first provides a complete description of the baseline model and its verification. Then, an extension of the 2D framework is proposed to model 3D phenomena by introducing permeability in the ice. Finally, ice accretion results are presented and discussed for four cases from the literature.

2. Computational Methodology of the Baseline Algorithm

The method borrows from the deterministic approach, presented in Section 2.1, which is always run prior to the stochastic process. It is used to compute the trajectories of the water droplets, as well as the thermodynamic balance for the water deposited on the exposed surface (in particular the solidification rate of the water). The proposed stochastic method is then called to change the ice shape, as described in Section 2.2. It is thus still based on the quasi steady-state assumptions used in ice accretion modelling, but it introduces stochasticity in the latter and enhanced interactions between water deposition and ice shape evolution. The latter is made possible by the advancing front algorithm presented in Section 2.3. The stochastic side of the process concerns the injection of the droplets (Section 2.4). In rather warm conditions, some water runback occurs on the iced surface. Section 2.5 explains how the deterministic calculation is used in the stochastic framework and how the advancing front algorithm is adapted to deal with water runback. Finally, the evolution process of the ice shape is stopped when a criterion, also derived from the deterministic calculation, is fulfilled (Section 2.6). After the verification presented in Section 2.7, some results of ice accretion on literature test cases are presented in Section 2.8.

2.1. Deterministic Framework

The developments of the stochastic method are implemented in the new Computational Fluid Dynamic (CFD) solver named CHApel Multi-Physics Simulation (CHAMPS) (Parenteau et al., 2021). It is developed at Polytechnique

Montreal using the Chapel programming language (Chapel, 2022), enabling native shared and distributed memory parallelizations of the software. Here, a brief overview of its features is presented with a focus on the icing modules; a more detailed description of the software can be found in (Parenteau et al., 2021). It performs unstructured simulations in 2D, 2.5D, and 3D using the finite volume method to solve the Reynolds-Averaged Navier-Stokes (RANS) equations, closed by the Spalart-Allmaras (Spalart and Allmaras, 1992) or the K-ω SST-V (Menter, 1992) turbulence models. The flux discretization follows Roe (Roe, 1981) or AUSM (Blazek, 2015) schemes and the second-order of accuracy is enabled using the Green-Gauss or Weighted Least Square gradient formulations (Blazek, 2015).

The icing framework follows the flowchart presented in Figure 3. It assumes a quasi-steady phenomenon: the flow and droplet fields, as well as the thermodynamic exchanges and the geometry evolution, are resolved in a steady-state fashion and the resolution assumes a one-way coupling between each module. The accuracy in time is increased using a multi-layer framework, the RANS mesh being regenerated at each quasi-steady iteration using a hyperbolic mesh generation algorithm (Chan, 1999).

An Eulerian droplet model is used to resolve the impingement map at the wall (Bourgault et al., 1999), with an upwind scheme for the convective fluxes and the same gradient formulations as the flow solver (Parenteau et al., 2021). The thermodynamic exchanges are obtained from an Iterative Messinger model (Zhu et al., 2012; Lavoie et al., 2016), and the geometry evolution is performed using either a Lagrangian (or algebraic) method, or a hyperbolic scheme (Bourgault-Côté, 2019).

2.2. Global Stochastic Process

The proposed stochastic method corresponds to a geometry evolution module, thus replacing its deterministic counterpart. The methodology, the results and the figures presented in the following sections were originally reported in the work of Papillon-Laroche (2022). The method is based on the discrete

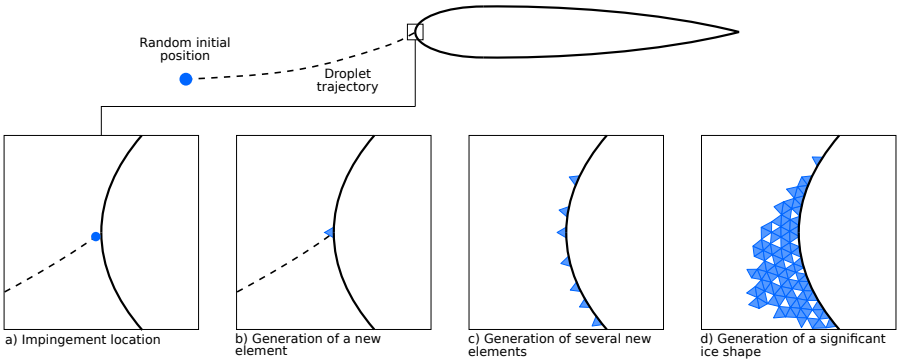

Figure 2: Global stochastic process

representation of the accretion domain by individual elements of ice, as proposed in (Szilder and Lozowski, 2004; Bourgault-Côté, 2019; Papillon-Laroche et al., 2021). However, the approach breaks with the Cartesian grid framework originally proposed by Szilder and Lozowski (2004), as it uses an unstructured advancing front mesh generator, enabling a body-conforming method. The cells of the created mesh represent the elements of ice.

An element of ice is generated from the incoming mass of water, as illustrated in Figure 2. The droplets are injected, one at a time, upstream of the studied geometry at a random position. The impingement location on the clean or iced geometry is computed using the droplet trajectory, which is extracted as a streamline of the deterministic droplet velocity field, knowing that the particle trajectories and streamlines coincide in the steady-state assumption. To reduce the computational cost, the droplets are gathered in clusters of mass $m_{cluster}$ in [kg], as proposed by Szilder and Lozowski (2004) : it is assumed that the droplets forming a cluster follow the same trajectory. The cluster mass is related to the ice element volume as presented in Section 2.3.

The cluster of droplets freezes either at the impingement location on the ice front or further downstream. It depends on the thermodynamic state at the cluster's current location, taken as its freezing fraction f_{fr}. The latter is obtained from the resolution of thermodynamic exchanges in a deterministic

fashion on the clean geometry, before the stochastic computations. When the thermodynamic state is favorable, a new element of ice is generated using the unstructured advancing front algorithm. The process stops when the accreted ice mass reaches the targeted ice mass (i.e., the stop criterion), as presented in Section 2.6.

Figure 3 illustrates the deterministic and stochastic icing frameworks in CHAMPS. The airflow, the droplet field, and the thermodynamic exchanges are resolved before the stochastic geometry evolution module (Figure 3a), in the same fashion as the deterministic framework (Figure 3b). This means that these solutions are available for the stochastic computations. Furthermore, Figure 3a shows that the stochastic method corresponds to a single-layer framework, contrary to the multi-layer deterministic solver. However, it accounts for the effects of the dynamic evolution of the ice front on the droplet trajectories in a finer way than the multi-layer simulations. Also, it could be considered to include this process in a multi-layer approach by extracting a meshable iced surface at the end of the stochastic process.

2.3. Unstructured Advancing Front Algorithm

The proposed method aims to model the icing phenomenon using a piecewise accretion process. Since the ice growth is a dynamic evolution, an unstructured advancing front algorithm is proposed, following the works of Bourgault-Côté (2019) and Papillon-Laroche et al. (2021).

2.3.1. General Process

The unstructured advancing front is typically used as a mesh generator. The method is based on the dynamic generation of triangular (2D) or tetrahedral (3D) elements from topological entities called the front facets. Here, the framework is in 2D and follows the methods of Lohner and Parikh (1988), Peraire et al. (1992) and Jin and Tanner (1993).

The discretization of the boundaries, e.g., the geometry walls and the farfield, forms the initial front as presented in Figure 4a in red. The front facets cor-

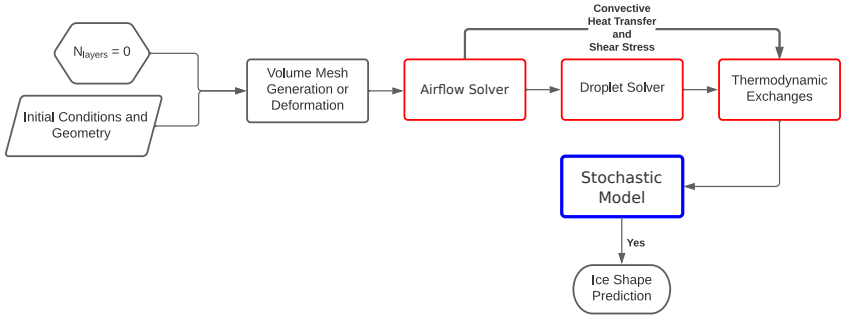

(a) Stochastic framework

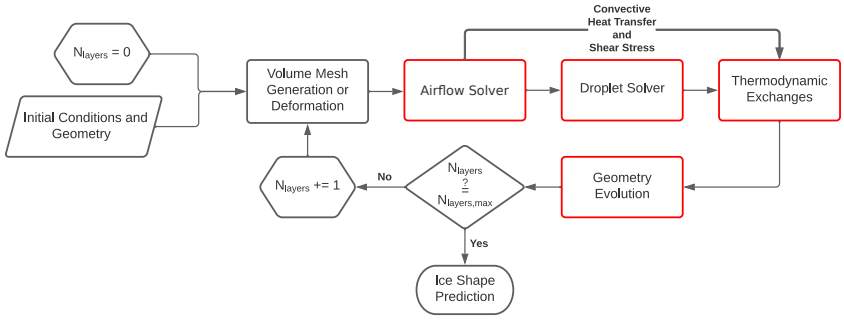

(b) Deterministic framework

Figure 3: Differences between the icing frameworks implemented in CHAMPS.

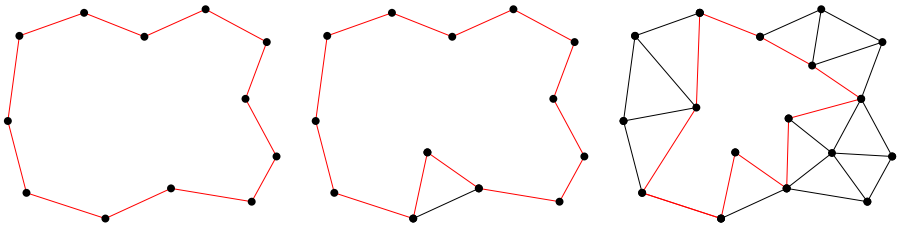

(a) Initial front

(b) Generation of one element and update of the front

(c) Front and mesh after several iterations

Figure 4: Unstructured advancing front process. The front is represented in red.

respond to the surface elements available to form a new volume element. The process goes as follows (Lohner and Parikh, 1988):

1. Select the next front facet to be treated following a predefined order of treatment.
2. Generate a new element, as illustrated in Figure 4b:
   (a) Select an existing front node in the neighbourhood of the selected facet or create a new node;
   (b) Check the validity of the new element (i.e., check for intersections with existing elements). If the element is invalid, return to step (2a).
3. Update the active front (Figure 4b, in red) :
   (a) Remove the treated facet;
   (b) Add the created facets.
4. Repeat steps 1 to 3 until reaching the stop criterion (Figure 4c), which is usually when the front is empty.

Generation of new elements. From the selection of the next front facet to be treated, an element can be generated either with an existing node or a new node. To that end, a search of front nodes is performed in the neighborhood of the optimal node position, denoted P_{opt} :

$$P_{opt} = P_{facet} + \frac{\delta\sqrt{3}}{2}\vec{n}_{facet} \tag{1}$$

where P_{facet} and $\vec{n}_{facet}$ are respectively the center of the selected front facet and its unit normal, and δ is the targeted element size in [m]. Since the method aims to generate as much as possible regular elements (equilateral triangles), P_{opt} is set to form an equilateral triangle of a side length of δ with a regular front facet, hence the term $\frac{\delta\sqrt{3}}{2}$ (i.e., the height of the corresponding equilateral triangle) in Equation 1.

The search of front nodes is performed around P_{opt} within a radius of 0.75δ, following the methodologies presented in (Lohner and Parikh, 1988; Peraire et al., 1992; Jin and Tanner, 1993). The validity of the elements formed by the treated facet and each resulting neighbor node is tested so that the new element does not intersect with any existing elements of the mesh. If there is more than one valid potential element, the most regular is selected to form the new element. If none of the neighbor front nodes form a valid element, a new node is created and a new valid element is generated with the latter.

2.3.2. Application to Icing

The key component of the method for the present icing application is the dynamic evolution of the front: the active front represents the ice front, which advances in space as the ice grows from the clean geometry. Additionally, specific phenomena, namely the variable ice density and the formation of shadow zones, are captured by the technique. Thus, the following features are of interest:

- Initial front;
- Order of treatment of the front facets;
- Creation of a new node and selection of an existing node;
- Element size.

Initial front. The initial front corresponds to the surface discretization of the studied geometry. A uniform surface mesh is created, based on the same geometry as the RANS mesh, using Pointwise (Pointwise, 2022). This ensures the regularity of the surface discretization required by the algorithm to converge,

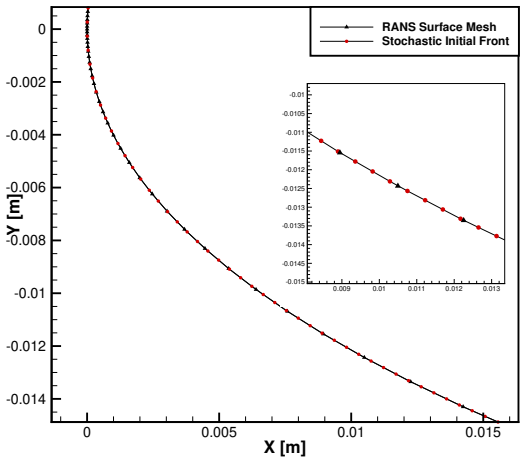

Figure 5: Comparison of the initial front and RANS surface mesh on the lower surface of a NACA0012

i.e., to reach the stop criterion with a complete and valid mesh. Additionally, it allows better control over the targeted element size of the ice mesh, independently of the surface discretization used for the RANS mesh generation. The comparison between the uniform surface mesh and the RANS surface mesh is presented in Figure 5.

Order of treatment of the front facets. When a cluster is injected into the computational domain, the intersection between its trajectory and the active front corresponds to the impingement location. This point is located on a front facet. For a rime thermodynamic state, i.e., $f_{fr} = 1.0$, the latter corresponds to the next front facet to be treated. For a glaze thermodynamic state, i.e., $f_{fr} < 1.0$, a fraction of the cluster flows further downstream on the ice front, requiring querying the thermodynamic state at each step of the cluster motion. Additional details on the freezing process are presented in section 2.5.

This process allows considering the ice front as a boundary (i.e., an obstacle) to the droplet impingement. Therefore, the shadowing effect of the growing ice is taken into account, contrary to the method of Bourgault-Côté (2019) or in single-layer deterministic approaches. Figure 6 illustrates this features. At a

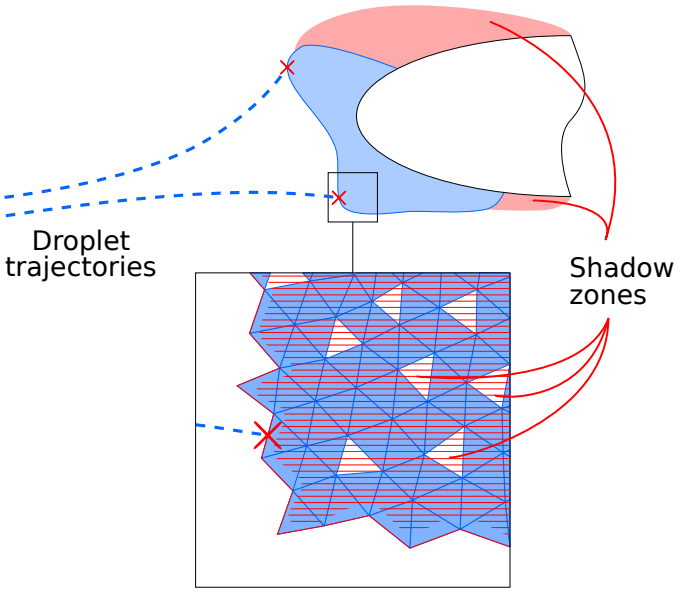

Figure 6: Shadow zones

macroscopic scale, it enables to better model the shadow zones behind ice horns. At a mesoscopic scale, it contributes to the formation of porosities within the ice, as described in the following paragraph.

Creation of a new node and selection of an existing node. The generation of a new element requires either the creation of a new node or the selection of an existing one. The former situation enables to advance the ice front in space, while the latter can lead to the generation of porosities within the ice, as illustrated in Figure 7. This is due to the creation of a second front, corresponding to the boundaries of the porosity (dashed red lines in Figure 7), as the main ice front (solid red lines in Figure 7) closes on itself. After their creation, the boundaries of the porosities can not be impinged again, resulting in a variable ice density.

Element size. The targeted element size δ controls the element size over the entire mesh, as well as the mass of the seeded cluster $m_{cluster}$ in [kg]:

$$m_{\text{cluster}} = \frac{\delta^2\sqrt{3}}{4} \cdot \rho_{ice,pure} \cdot b$$

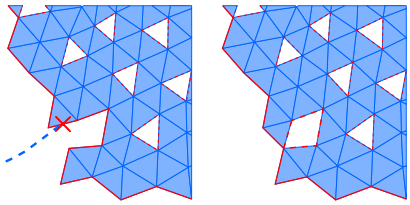

Figure 7: Creation of an air pocket

where $\rho_{ice,pure} = 917$ kg/m^3, corresponding to the pure ice density (Szilder and Lozowski, 2004), and $b = 1.0$ m represents the span to respect the units in this 2D framework. The term $\frac{\delta^2\sqrt{3}}{4}$ represents the area of a equilateral triangle of side δ.

2.4. Impingement Process

To obtain the impingement location required by the advancing front algorithm, the droplet trajectories are extracted as the streamlines of the droplet velocity field computed by the deterministic Eulerian solver. Hence, the trajectories are computed using the RANS volume mesh, since the Eulerian droplet velocity field is obtained for the latter discretization. The complete process corresponds to an adaptation of the finite volume representation of the streamlines proposed by Rendall and Allen (2014). Following the assumption that the droplets forming a cluster have the same evolution, the cluster trajectory corresponds to the trajectory of a single droplet subjected to the same conditions.

2.4.1. Global Process

The process is illustrated in Figure 8 and goes as follows:

1. Insert a cluster of droplets at a random position $P_{d,0}$ on a seeding plane, upstream of the studied geometry.
2. Identify the initial cell of the RANS mesh in which the cluster is seeded, using an octree geometric search algorithm (Press et al., 2007).
    - The cluster's initial position, $P_{d,0}$, corresponds to its entry point, $P_{d,entry}$, in the initial RANS cell (Figure 8a).

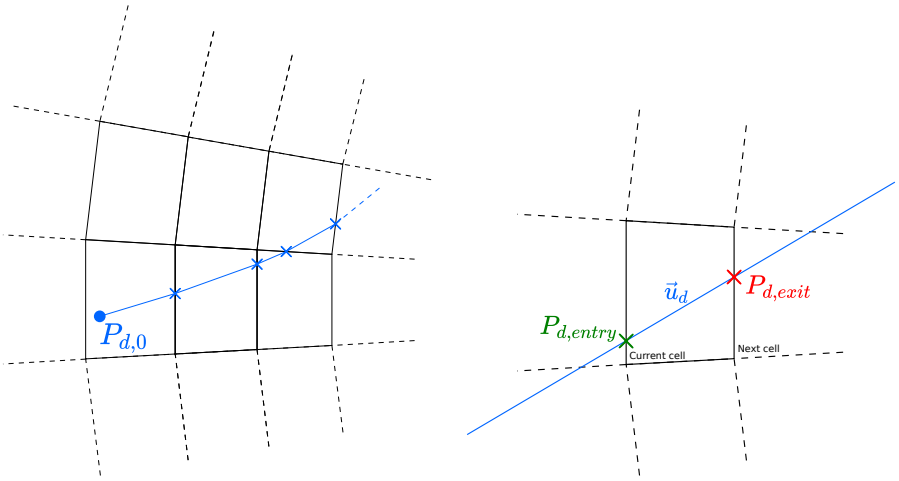

(a) Droplet trajectory (in blue) in the RANS mesh (in black).

(b) Facet/velocity ray intersection computations in the current cell (in black).

Figure 8: Droplet trajectory computation

3. Compute the cluster's exit point, $P_{d,exit}$, of the current RANS cell (Figure 8b):
   (a) Retrieve the droplet velocity $\vec{u}_d$ from the current RANS cell.
   (b) Compute the intersection between the velocity ray (formed by $\vec{u}_d$ and passing by $P_{d,entry}$) and the facets of the cell (obtained from the cell-to-facets connectivity list).
   - $P_{d,exit}$ corresponds to the intersection point in the same direction as $\vec{u}_d$:

$$(P_{d,exit} - P_{d,entry}) \cdot \vec{u}_d > 0$$

   (c) With the cell-to-cells connectivity list, identify the next RANS cell along the streamline:
   - It corresponds to the cell on the other side of the intersected facet.
   (d) Return to step 3(a), using the $P_{d,exit}$ of the current cell as the $P_{d,entry}$ in the next cell : $P_{d,entry} = P_{d,exit}$.

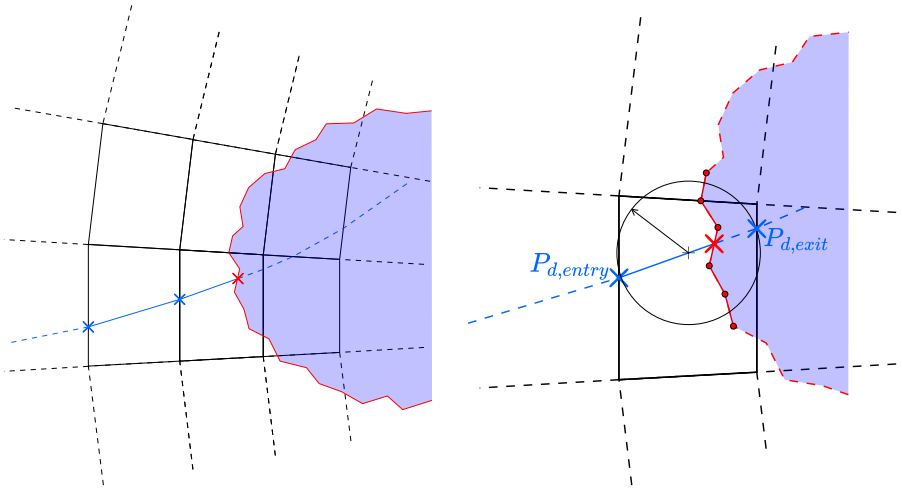

(a) Droplet trajectory intersection with the ice front

(b) Intersection check zoomed

Figure 9: Computation of the impingement location

The process stops if either the clean geometry wall or the active ice front is intersected. Both cases are treated in the same way as the clean geometry is represented by the initial front. When the trajectory is close to the ice front, a geometric search is performed around the current volume cell being crossed. To that end, an intersection check between the trajectory and the facets within a search radius of $r = 0.5\ ||P_{d,exit} - P_{d,entry}||$ of the coordinate $P_{d,entry} + r$ is performed, as depicted in Figure 9b. The impingement location corresponds to the intersection between the ice front and the droplet trajectory, and the intersected front facet is the impinged facet. An octree is used to reduce the cost of such a geometric search.

A similar approach is presented in the work of Butnarasu et al. (2015). However, in the latter approach, the ice accretion domain is discretized by a complete Cartesian grid, and the droplet streamlines are extracted for each visited cell of the Cartesian grid, requiring both interpolation of the droplet velocity (from the RANS mesh to the Cartesian grid) and the integration of the streamline at each step (i.e., at each visited cell). The process proposed in

the present paper does not require any interpolation or integration due to the finite volume representation of the streamline which simply corresponds to its geometric representation.

It is worth justifying the use of the Eulerian droplet velocity field to retrieve $\vec{u}_d$, instead of resolving the droplet equations of motion within a Lagrangian particle tracking method:

- The Eulerian droplet impingement model computes the impingement map on the clean geometry. This allows to extract the impingement limits on the surface and retrieve the seeding limits on the seeding plane, as described in Section 2.4.2. Therefore, the insertion of the clusters is limited to a seeding window and the computational cost associated with the clusters not impacting the ice front is reduced. Additionally, the clusters are injected on a seeding plane positioned upstream of the geometry, at about one chord length of the leading edge. The only restriction on its position is to ensure that the clusters are always seeded upstream (in front) of the ice. In other words, it only has to accommodate the growth of the ice contrary to a traditional Lagrangian particle tracking method, which requires the droplets to be seeded where they are subjected to the free stream conditions (Erhan et al., 2011).

- The thermodynamic exchanges over the surface are computed according to the impinging water mass rate on the clean geometry, obtained from the Eulerian solver. This allows to establish :

  1. the thermodynamic state for each cluster and the corresponding mass of water to be frozen using the computed freezing fraction, as detailed in Section 2.5;
  2. the stop criterion of the process using the computed ice mass rate, as detailed in Section 2.6.

  This process is consistent with mass conservation.

The proposed impingement process would also be compatible with a Lagrangian particle tracking method, but further developments would be needed to establish a consistent stop criterion.

2.4.2. Seeding Process

The seeding plane is parallel to the vertical axis, denoted y, and its position along the x-axis is given as an user input : $x = p_{seed}$. Thus, the initial position of a cluster is : $P_{d,0} = (p_{seed}, y_{d,0})$. The coordinate y-component $y_{d,0}$ is randomly generated in a seeding window using a Pseudo Random Number (PRN) generator.

Seeding window. To reduce the computational cost of the impingement process, the number of clusters not impinging the ice front is limited due to the computation of a seeding window, meaning that :

$$y_{d,0} \in [y_{d,min}, y_{d,max}]$$

These extremum values are obtained from impingement limits on the surface. Indeed, the process computes the upstream trajectories from the two positions on the clean geometry where the collection efficiency β (computed by the Eulerian solver) reaches the condition $\beta < \varepsilon$, where $\varepsilon = 10^{-8}$ in this paper, as illustrated in Figure 10. Their computation follows the steps presented in Section 2.4.1, but instead of selecting the intersection point in the same direction as $\vec{u}_d$ at step 3(b), the one in the opposite direction is selected as the exit point (Rendall and Allen, 2014):

$$(P_{d,exit} - P_{d,entry}) \cdot \vec{u}_d < 0$$

The intersection of the upstream trajectories with the seeding plane gives the interval $[y_{d,min}, y_{d,max}]$. Finally, to ensure a sufficient seeding window (i.e., the entire ice front can receive water) as the ice grows into significant ice structures, the interval's endpoints are shifted so that the window size is extended by at least 50%. The extended seeding window is denoted $[y'_{d,min}, y'_{d,max}]$.

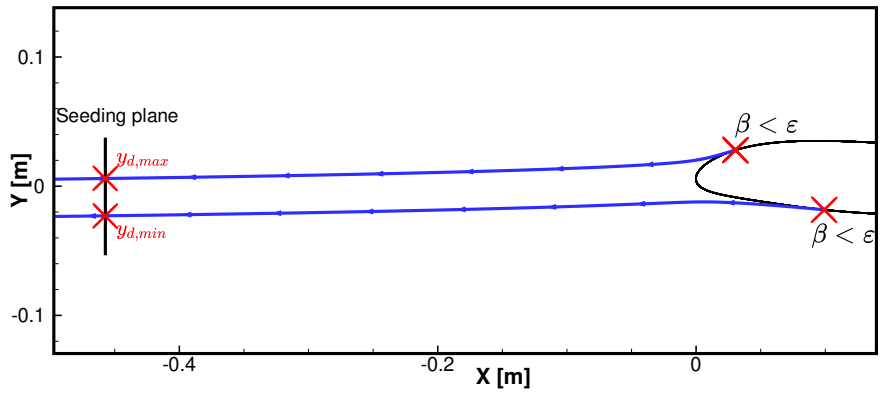

Figure 10: Seeding plane position and limits obtained from the upwind droplet trajectories of the impingement limits

The pseudo-random initial position $y_{d,0}$ on the seeding plane is then generated in the interval $[y'_{d,min}, y'_{d,max}]$ using a Permuted Congruential Generator (PCG) (O'Neill, 2014), available in the Chapel language as a standard library (Chapel, 2022). The PCG is based on the generation of PRNs with a medium-quality PRN generator. Then, the quality of the generated PRNs' are improved using a permutation function, resulting in PRNs of good statistical properties (period, uniformity, and predictability). The reader is referred to (O'Neill, 2014) for more details on this PRNs generator. The PRNs are generated following a uniform probability density function, as the spatial distribution of the droplets in a cloud is considered to be uniform (Shaw et al., 2002).

Droplet Size Distribution Treatement. The other source of stochasticity in the icing phenomenon considered in the proposed method is the variation of the size of the droplets throughout the cloud. To that end, using the experimental droplet size distribution, the diameter of the droplets in a given cluster is generated using the inverse transform sampling method (Sugiyama, 2016). A cluster is formed by droplets of the same size; the stochasticity of the droplet sizes throughout the cloud is introduced by randomly selecting the droplet diameter associated to a given cluster following the experimental droplet size distribution.

The droplet size distribution is often given as the cumulative fraction of the liquid water content (LWC) according to the droplet diameter in a discrete form, as illustrated in Figure 11. In the deterministic framework, the Eulerian droplet trajectory model solves the velocity field for each droplet diameter and the resulting collection efficiency is the weighted average of the collection efficiencies computed for each droplet diameter (Lavoie, 2017). In the proposed stochastic framework, the size of the droplets forming a cluster is randomly generated for each seeded cluster. The inverse transform sampling method allows generating a random sample from a given discrete cumulative density function (CDF) following the associated probability density function (Sugiyama, 2016). The process is illustrated in Figure 12. Either the experimental droplet size distribution or an empirical distribution, such as the Langmuir D presented in Figure 11, is used as the discrete CDF. The Eulerian velocity fields are obtained for the same distribution. Each droplet diameter i of the discrete size distribution is associated with a sub-interval I_i of the cumulative LWC fraction. Then, a uniform pseudo-random number $u \in [0, 1]$ is generated using the PCG, and the interval I_i for which $u \in I_i$ is found. The randomly sampled droplet diameter corresponds to the diameter i.

Finally, once the cluster formed by droplets of the randomly sampled diameter is seeded, the trajectory is computed using the corresponding velocity field obtained from the same droplet diameter with the Eulerian droplet trajectory model. Here, it is worth noting that the cluster mass does not change as it is associated only with the element size in the advancing front technique.

2.4.3. Verification of the Droplet Trajectory Model

The stochastic impingement maps for two test cases are compared against the deterministic results of CHAMPS. The selected cases are Cases 241 and 364 of the first IPW (Laurendeau et al., 2022) and the corresponding icing conditions are given in Table 1.

The collection efficiency is computed for both methods on the clean surface, i.e., there is no ice accumulated to allow a direct comparison between the results.

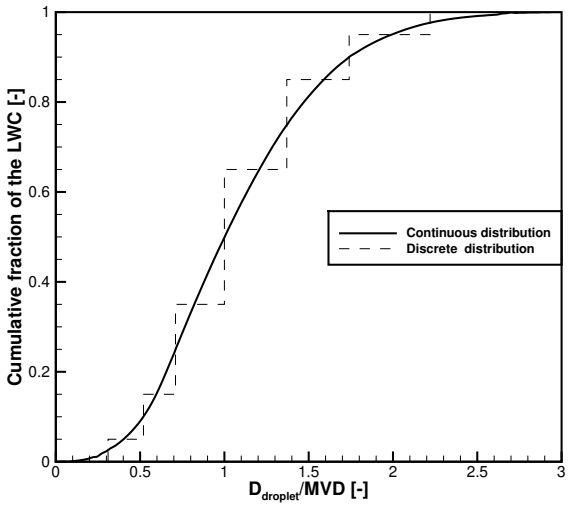

Figure 11: Langmuir D distribution with the data extracted from (Papadakis et al., 2007)

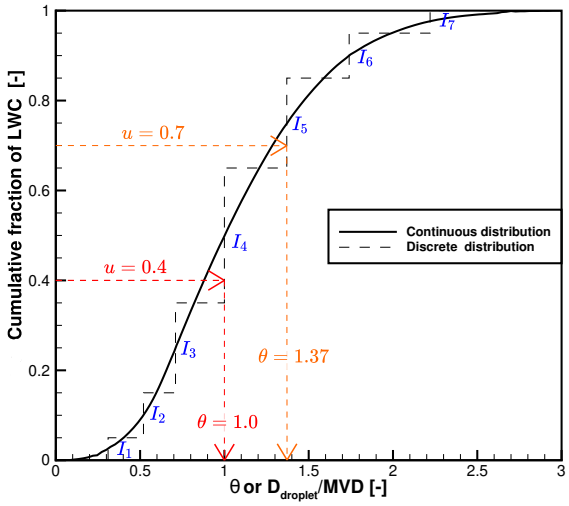

Figure 12: Inverse transform sampling

For Case 241, a monodispersed size distribution is considered, while Case 364 considers the experimental size distribution, given in (Laurendeau et al., 2022).

The stochastic collection efficiency is obtained from its Lagrangian definition:

$$\beta_{i,stoch} = \frac{n_{i,imp}\, m_{cluster}}{\Delta s_i\, \Delta t_{icing}\, U_{inf}\, \mathrm{LWC}}$$

where $\beta_{i,stoch}$ is the collection efficiency for the front facet i, Δs_i is its area in $[m^2]$ and $\Delta s_i = l_i \cdot b$ with l_i being the length of the facet in [m], $n_{i,imp}$ is the number of clusters that have impinged the facet i, and Δt_{icing} and U_{inf} are respectively the icing time in seconds and the magnitude of the free stream velocity in m/s.

Figure 13 presents the results of β according to the arc length from the trailing edge (TE) for both cases: it shows that the stochastic impingement map represents the deterministic collection efficiency. Furthermore, stochasticity is observed in the distribution, which is expected for the proposed method. Additionally, the agreement between the stochastic and deterministic results of Case 364 in Figure 13b verifies that the droplet size distribution treatment is suitable. However, a decrease of β near its maximum value, which corresponds to the position of the stagnation point, is observed. This is assumed to be linked to dividing streamlines in this region when the RANS mesh cells are parallel to the streamlines. This occurs in Case 364 for which the flow is at 0^o angle-of-attack over a symmetrical geometry, as the RANS mesh used is a structured-type grid with the latter aligned with the flow direction in the symmetry plane. For this situation, the streamlines are driven away from the stagnation point resulting in a separation of the upper and lower trajectories near this point. A similar observation of this phenomenon is made by Porter (2022) for trajectories computed from a Lagrangian particle tracking algorithm. This leads to a shadow zone on the ice front where no cluster can impinge, as illustrated in Figure 14. This constitutes a limitation of the proposed method. The phenomenon has less impact on the collection efficiency obtained for Case 241 since an unstructured RANS mesh is used.

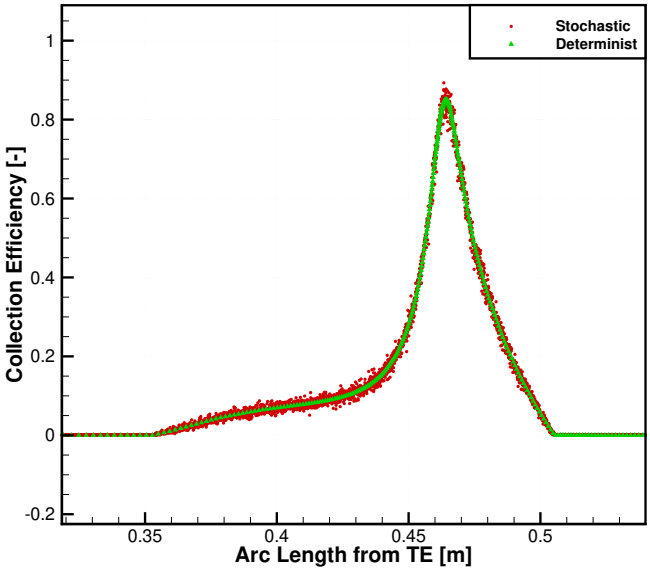

(a) Verification of the collection efficiency for Case 241 with $\delta = 1.25 \times 10^{-4}c$

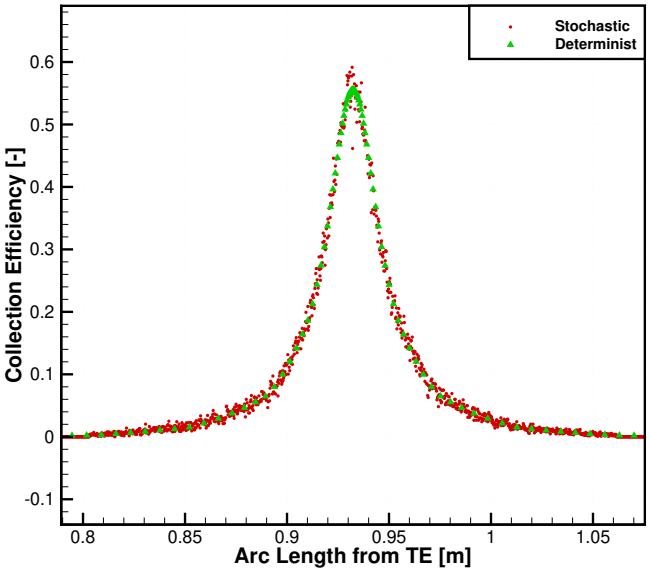

(b) Verification of the collection efficiency for Case 364 with $\delta = 2.5 \times 10^{-3}c$

Figure 13: Verification of the collection efficiency

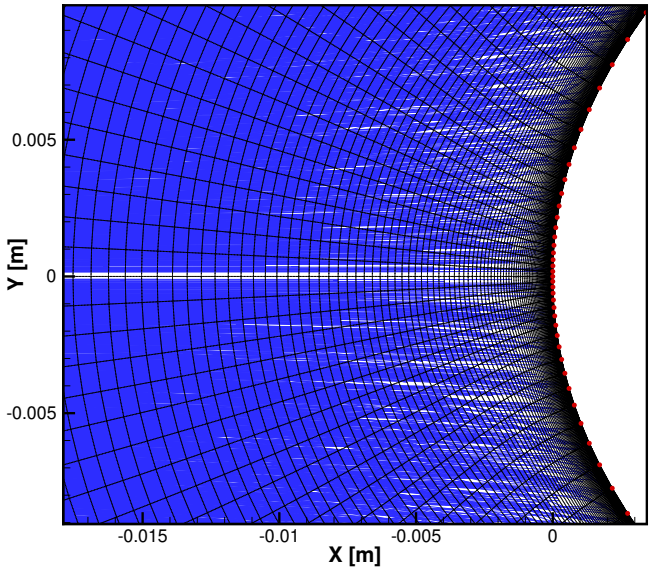

Figure 14: Limitation of the droplet trajectory computation. The trajectories are represented by the blue lines and the RANS mesh by the dotted black lines.

2.5. Freezing Process

The freezing process follows the impingement of a cluster and is significant for glaze icing cases. In such conditions, the cluster flows on the ice front from its impingement location in the same direction as the shear stress at the wall. The distance traveled depends on the thermodynamic state along the current front. This motion of the cluster on the clean/iced surface is also found in the other Lagrangian icing models (Szilder and Lozowski, 2004; Bourgault-Côté, 2019; Leroy, 2004; Butnarasu et al., 2015). The thermodynamic state is given by the freezing fraction f_{fr}. The front facets downstream of the impingement location are treated sequentially, enabling the modeling of the cluster motion on the active front.

2.5.1. Thermodynamic Exchanges

The freezing fraction is computed prior to the stochastic process using an Iterative Messinger model (Zhu et al., 2012) and is defined according to :

$$f_{fr} = \frac{\dot{m}_{ice}}{\dot{m}_{imp} + \dot{m}_{in} - \dot{m}_{es}} \tag{2}$$

where $\dot{m}_{ice}$, $\dot{m}_{imp}$, $\dot{m}_{in}$ and $\dot{m}_{es}$ are respectively the mass rates of accumulating ice, impinging water, incoming runback water and evaporation/sublimation. This approach is compatible with the quasi-steady approaches classically used for ice accretion modeling, for which it is assumed that all the liquid water flows according to the shear stress direction, and does not stagnate locally or soak the ice.

Equation 2 is adapted to the current framework with the two following considerations:

- The evaporation/sublimation mass rate is neglected, which was originally proposed as a simplifying assumption in the work of Leroy (2004). It is assumed to be negligible compared to the incoming mass rate.
- The mass rate terms in [kg/s] are replaced by mass terms in [kg], as a cluster of droplets corresponds to a given mass of water.

Therefore, Equation 2 is re-written according to :

$$f_{fr} = \frac{m_{ice}}{m_{imp} + m_{in}} \tag{3}$$

At each step of the cluster motion on the front, the value of the freezing fraction is approximated by its value at the nearest surface cell of the RANS mesh as the thermodynamic exchanges are resolved with the latter discretization (Bourgault-Côté, 2019). The mass of water to be frozen is then given by :

$$m_{ice} = f_{fr}(m_{imp} + m_{in}) \tag{4}$$

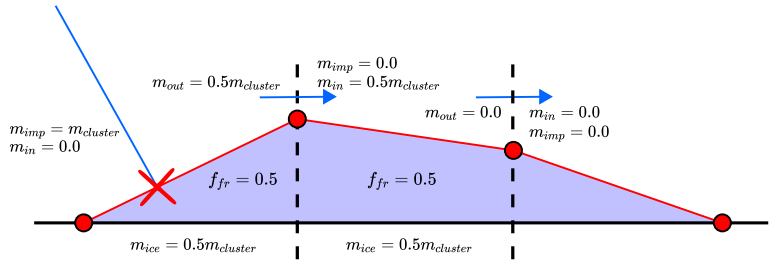

Figure 15: Cluster motion on the active front

2.5.2. Runback Modeling

The mass of liquid water running back to the next front facet is obtained from the mass balance at the surface of the current front facet:

$$m_{out} = m_{imp} + m_{in} - m_{ice} \tag{5}$$

This mass corresponds to the incoming mass m_{in} for the next front facet, as presented in Figure 15. It is important to note that for the steps of the cluster motion following the impingement, $m_{imp} = 0.0$ kg since the clusters are treated sequentially, i.e., there is no impinging water remaining on the front.

The next facet to receive the runback water m_{out}, referred to as the receiving facet, is selected as a direct neighbor of the current facet in the same direction of the shear stress at the front surface.

Runback direction. The runback water follows the direction of the skin friction coefficient $\vec{C}_f$ at the geometry surface, which is either clean or iced. Since the flow is not updated as the ice grows, $\vec{C}_f$ at the active ice front is unknown in the proposed method. However, it can be approximated to the skin friction coefficient at the nearest cell of the surface RANS mesh, which is computed prior to the stochastic method by the deterministic airflow solver. The approximated direction is therefore denoted $\vec{C}_f{}'$.

Selection of the receiving facet. The ice front being irregular and presenting concavities, the identification of which neighboring front facet is in the direction of $\vec{C}_f{}'$ is ambiguous, as illustrated in Figure 16a where the red 'X' marks the

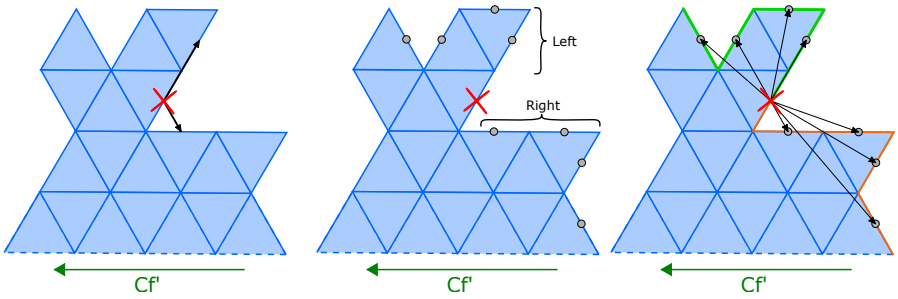

(a) Irregular ice front

(b) Stencil

(c) Selection of the appropriate runback side, in green

Figure 16: Selection of the next receiving facet

impinging location. Therefore, to select the receiving facet, the vectors between the impinged front facet and a 1D stencil of N neighboring front facets on the left and right sides of the impingement location are compared to $\vec{C_f}'$.

To do so, the scalar product between $\vec{C_f}'$ and the vector from the center of the impinged facet, $P_{facet,imp}$, to the center of the ith neighbor facet, $P_{facet,i}$, is computed. If

$$(P_{facet,i} - P_{facet,imp}) \cdot \vec{C_f}' > 0$$

the vectors point in the same direction. This process is illustrated in Figures 16b and 16c. The side for which there are more facets in the same direction of $\vec{C_f}'$ is selected as the runback side. This process is performed once, upon impingement, as it is assumed that the runback mass fraction of the cluster will always flow according to the same direction (i.e., the cluster cannot go back on its steps) until reaching the stop criterion.

Runback Stop Criterion. The runback process stops when the water outflow m_{out} computed with Equation 5 is negligible according to the following heuristic criterion:

$$m_{out} \leq 0.01 m_{cluster}$$

When the criterion is reached, the remaining mass is entirely given to the last visited facet, ensuring mass conservation. No proper parametric study was done for this criterion, as for the upcoming criterion in Equation 6. This could be done in the future, although the good results obtained afterwards and the fact that these are negligibility thresholds, suggest that the sensitivity to these criteria is low.

2.5.3. Generation of a New Element of Ice

The mass of water to be frozen at each step of the cluster motion is given by Equation 4. However, since the advancing front technique requires regularity in the size of the generated elements to converge (i.e., to result in a complete and valid mesh), the process generates a new element of ice only if :

$$m_{ice} \geq 0.9 m_{cluster} \tag{6}$$

which is an heuristic criterion. The latter is checked at each step of the cluster motion. If it is not reached, the ice mass given by Equation 4 is stored on the front facet (denoted $m_{ice,stored}$), and is considered the next time this facet is visited :

$$m_{ice} = f_{fr}(m_{imp} + m_{in}) + m_{ice,stored}$$

When the criterion is reached, a new element of ice is generated with the advancing front technique. The heuristic criterion given by Equation 6 aims to ease the advancing front technique by introducing some flexibility in the generated elements while keeping them mostly regular, especially when selecting existing nodes. Nonetheless, the mass conservation is ensured by the process.

2.6. Stop Criterion

The global process stops when the accumulated ice mass $M_{acc,ice}$ reaches the targeted mass $M_{total,ice}$. The latter is computed from the deterministic thermodynamic solution, and corresponds to the integral over the clean surface of the ice mass rate $\dot{m}_{ice}$:

$$M_{total,ice} = \Delta t_{icing} \int_S \dot{m}_{ice} ds$$

$$= \Delta t_{icing} \cdot \sum_{i=1}^{n} \dot{m}_{ice,i} \Delta s_i$$

where n corresponds to the number of surface elements of the RANS mesh and $\dot{m}_{ice,i}$ is the ice mass rate of the surface element i. $M_{acc,ice}$ is computed as the sum of the masses of the generated elements of ice :

$$M_{acc,ice} = \sum_{i=1}^{N} m_{\text{element},i} \tag{7}$$

where N is the total number of elements of ice, $m_{\text{element},i} = V_{\text{element},i} \cdot \rho_{ice,pure}$, corresponding to the mass of the ith element, and $V_{\text{element},i}$ is its volume.

2.7. Mesh Convergence Study

A convergence study on the element size δ is performed, while the RANS mesh remains unchanged. The ice density is selected as the study parameter since it is a dependent variable in the proposed method (Section 2.3.2). This was initially proposed by Bourgault-Côté (2019) and re-examined by Papillon-Laroche et al. (2021). Case 241 is selected as it represents rime icing conditions for which the ice density is variable, contrary to the glaze icing conditions in which it is typically $\rho_{ice,pure} = 917$ kg/m^3 . The accretion time is, however, decreased to 2.5 minutes to reduce the computational cost.

The values of the element size δ range from $1.0 \times 10^{-3}c$ to $6.25 \times 10^{-5}c$ with a refinement factor of two, and since the process is random, five trials are performed for each element size. The resulting ice meshes for a single trial of the first four element sizes are presented in Figure 17.

The ice density is extracted from a core sample at the leading edge of each obtained ice mesh and is denoted ρ_{ice}; more details on the ice density extraction can be found in (Papillon-Laroche, 2022). Since there is no analytical solution for this case, the exact value of the density is approximated to $\rho^*_{ice} = 753.81$ kg/m^3, which is the result on the finer mesh ($\delta = 6.25 \times 10^{-5}c$). For each element size, the ice density corresponds to the average of the five trials.

The convergence of the ice density according to δ is presented in Figure 18 and shows that the method converges. The slopes of the 1st- and 2nd-orders of

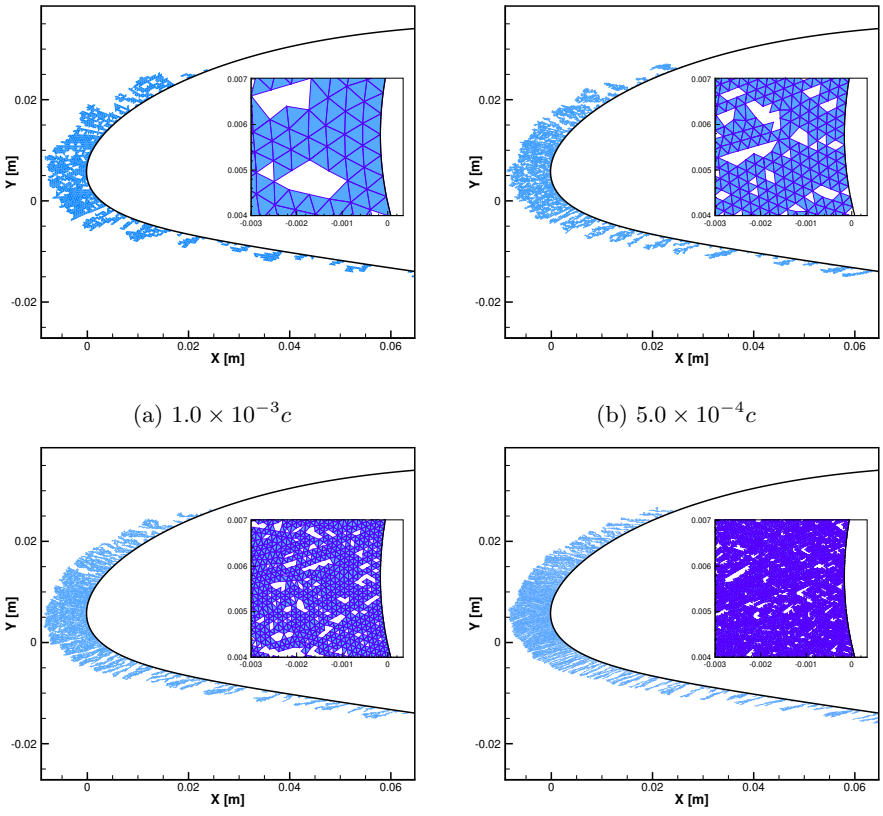

(a) $1.0 \times 10^{-3}c$

(b) $5.0 \times 10^{-4}c$

(c) $2.5 \times 10^{-4}c$

(d) $1.25 \times 10^{-4}c$

Figure 17: Element size effect on the ice shape

accuracy are only depicted for reference purposes, as there is no formal order of convergence for the proposed method.

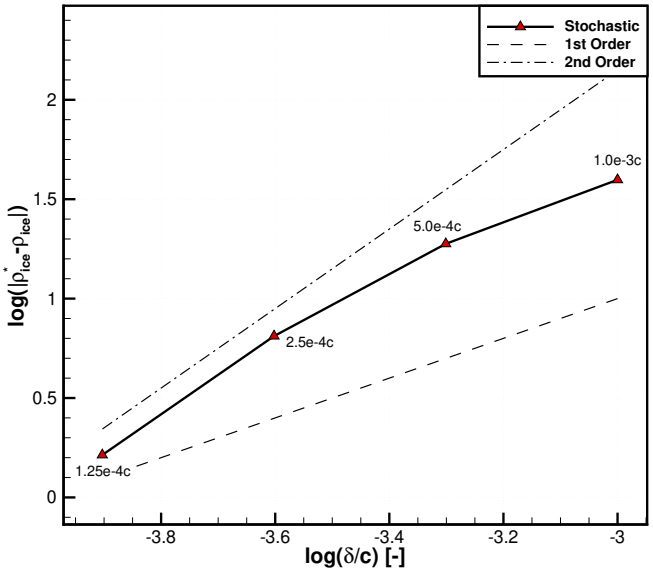

Figure 18: Ice density convergence study

2.8. Results of the Baseline Algorithm

The ice shape for a single trial of Case 241 obtained from the baseline algorithm is presented in Figure 19. The stochastic ice shape, in blue, is compared to the inner and outer envelops of the scan of the experimental ice (Laurendeau et al., 2022), in green, and to the 5 layers deterministic result of CHAMPS. The stochastic method successfully captures discrete ice structures and a variable ice density. However, Figure 19 shows that the ice thickness of the stochastic result is overestimated. The deterministic computations, which lead to an ice thickness in the expected range, are resulting from the use of a constant ice density of $\rho_{ice} = 820.0$ kg/m^3, while in Section 2.7, the mesh convergence study results in a stochastic ice density of 753.8 kg/m^3. This suggests that the latter is too low compared to the experimental value.

This assumption can also be made for the regions in which discrete ice structures (i.e., ice feathers) are observed. This is mainly the case for the low surface, downstream of the stagnation point. A numerical amplification of the feather formation is also suspected, as they are very long and thin, compared to the voids separating them. The final shape of the ice in this region suggests their formation is mainly driven by the first ice elements accumulated at the clean surface.

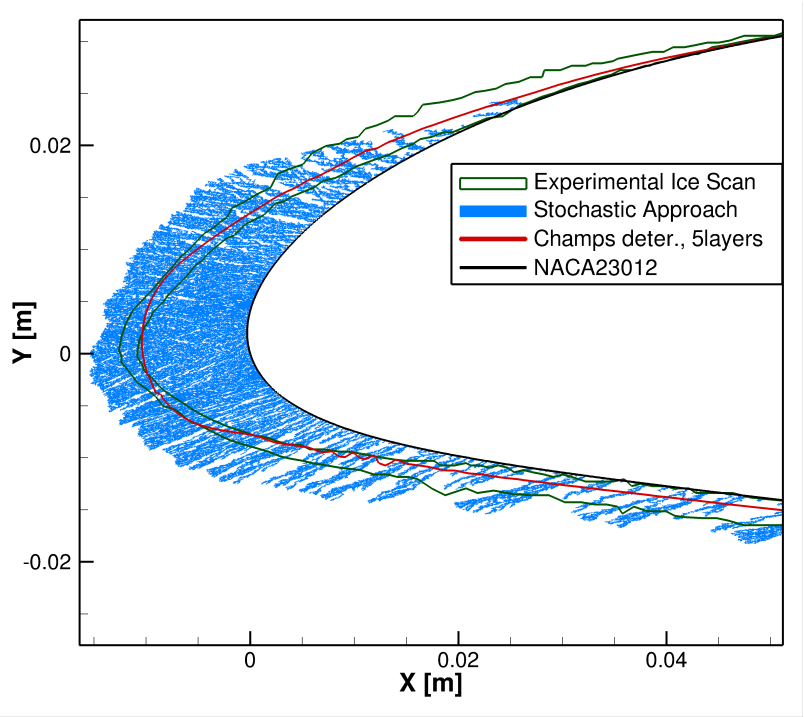

Figure 19: Initial results for Case 241, $\delta = 1.25 \times 10^{-4} c$

A lower ice density was also reported in the works of Szilder and Lozowski (2004) and Leroy (2004). To increase it, Szilder and Lozowski (2004) proposed a cradle search, which allows a cluster to freeze beyond its freezing location. This method emulates the surface tension effect, which drives the water's tendency to fill voids. The cradle search is performed in a radius of N times the Cartesian cell size of the freezing location, resulting in a method dependent on the

Cartesian discretization. Leroy (2004) proposed a similar approach, allowing a fluid element to flow over a given distance after it reaches its freezing state.

3. Improved Algorithm

Here, an improved algorithm is presented to take into account the assumed 3D nature of the ice density, and to avoid the suspected numerical amplification of the ice feathers.

In the real icing phenomenon, the ice varies along the three axes of the reference frame: in the chordwise direction x, along the vertical axis y, and in the spanwise direction z. This is ignored in the presented 2D framework unless one considers that various trials correspond to different z-sections. The effect on the ice shape is assumed to be significant in light of the results presented in Figure 19. Indeed, if three droplets are seeded at respectively $(x_{d,0},\ y_{d,0},\ z_{d,0}+\varepsilon)$, $(x_{d,0},\ y_{d,0},\ z_{d,0})$, and $(x_{d,0},\ y_{d,0},\ z_{d,0}-\varepsilon)$, where ε corresponds to a small distance, their respective impingement position on the ice front can be significantly different, as illustrated in Figure 20. This is however not captured by the approach of the previous section because the trials are strictly independent and it is then not possible to realistically assign three trials respectively to $z = z_{d,0}+\varepsilon$, $z = z_{d,0}$ and $z = z_{d,0}-\varepsilon$.

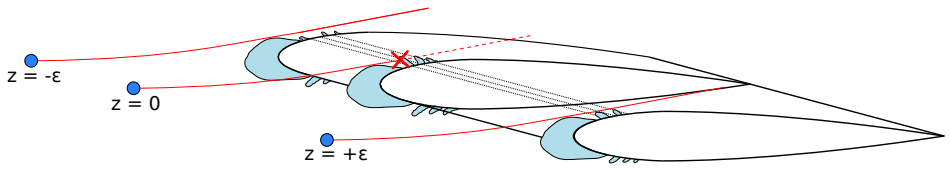

Figure 20: Interpretation of the effect of the spanwise direction

Therefore, to take into account this effect in the spanwise direction, the ice front of a given trial is considered to be permeable to a certain extent, allowing some clusters to impinge behind the main ice front in an air pocket. Figure 21 shows this permeable front technique, which goes as follows for a given cluster:

1. Compute the impingement location, denoted $P_{imp,0}$, as presented in Section 2.4;
2. For each intersection $P_{inter,current}$ with a front facet facing upstream ($\vec{n}_{facet} \cdot \vec{u}_d < 0$) along the cluster trajectory :
   (a) Generate a uniform PRN of either 0 (false) or 1 (true) :
      - **If** PRN = 1, the current cluster intersection with the ice front corresponds to the impingement location. Continue to the freezing process described in Section 2.5;
      - **Else** (PRN = 0), compute the distance d between $P_{inter,current}$ and $P_{imp,0}$:
        - **If** $d \leq d_{max}$, where d_{max} is a user-defined parameter, continue to the next intersection (step 2).
        - **Else** ($d > d_{max}$), discard the cluster and continue with the injection of a new cluster upstream.

The PRN is generated using the PCG (O'Neill, 2014).

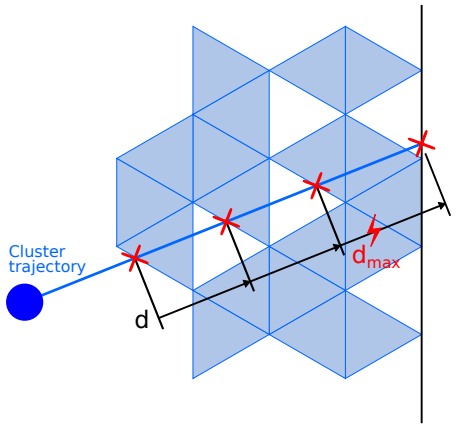

Figure 21: Process to emulate the permeability of the ice front. The intersections of the trajectory with a front facet facing upstream are marked by a red 'X'.

The parameter d_{max} does not have any physical meaning, thus requiring a proper calibration to ensure the spatial convergence and the validity of the model with this proposed extension. Figures 22 and 23 present the sensitivity

of the ice shape to the values d_{max} ranging from $5.0 \times 10^{-4}c$ to $3.2 \times 10^{-2}c$, with a scaling factor of 2. The light blue zone represents the projection in the xy-plane of the spanwise experimental ice. The results show that the ice density increases with the value of d_{max}, because more clusters are deposited in air pockets, resulting in a decrease in the ice thickness. Also, the geometry of the ice feathers changes, starting with long and thin structures at the lower values of d_{max} and ending with shorter and thicker structures accreted closer to each other for the highest values of the range. This shows that the method allows, for a given trial in the considered 2D plane, to model well the fact that the feathers can thicken due to the deposition of water droplets seeded from a very close plane. Qualitatively, the values in the interval $d_{max} = [5.0 \times 10^{-4}c, 2.0 \times 10^{-3}c]$ lead to ice shapes in better agreement with the experimental results than the baseline algorithm ice shape reported in Figure 19.

Finally, it is important to note that the permeable front technique is not intended to replace the stochastic model extension to a fully 3D framework. However, the improvement of the results showed in Figure 22 justifies such an extension to capture phenomena missed by the 2D framework.

4. Results and Discussion

The icing conditions of the test cases selected for the validation of the proposed model are provided in Table 1. The computational domain for the NACA0012 geometry is discretized with a structured O-type grid and has 384x256 cells. The far-field is located at 50 chords. An unstructured mesh is used for the NACA23012 cases, based on the wind-tunnel configuration provided by the IPW (Laurendeau et al., 2022). The airfoil and wind tunnel walls are discretized with respectively 778 and 198 vertices for a total of 68000 cells. For both meshes, the height of the first cell is at $y^+ < 1$. For each case, the flow and droplet solvers reach a density residual reduction of 10^{-5}.

The value of d_{max} chosen for each case is based on sensitivity studies similar, yet not as extensive, as the one presented in the previous section. d_{max} is thus

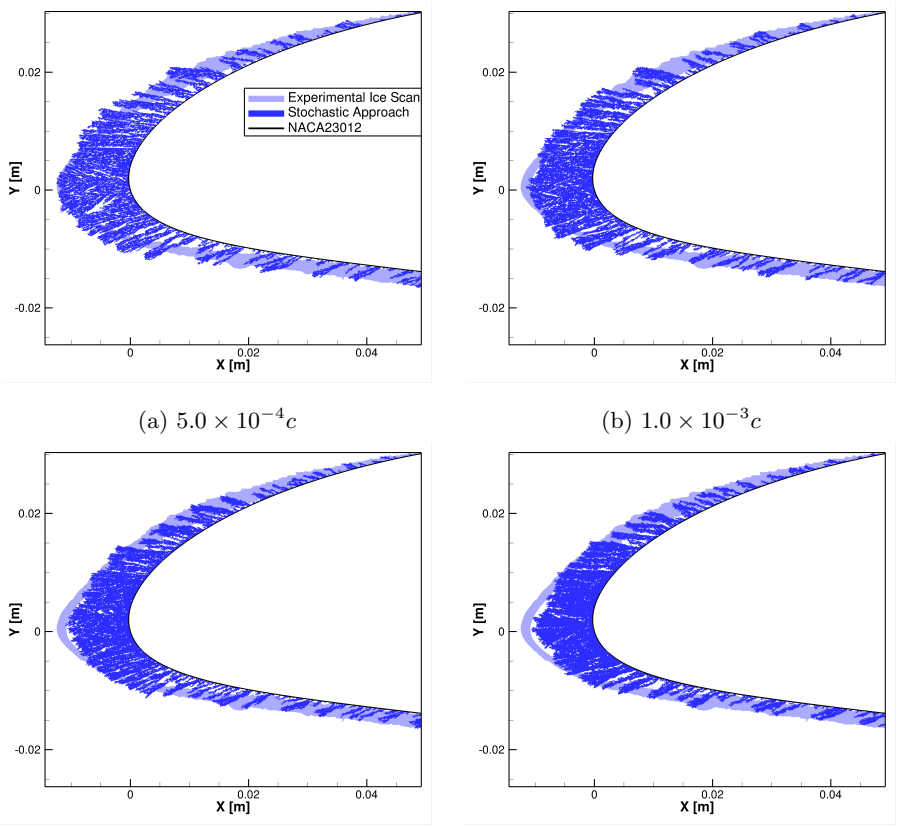

(a) $5.0 \times 10^{-4}c$ (b) $1.0 \times 10^{-3}c$

(c) $2.0 \times 10^{-3}c$ (d) $4.0 \times 10^{-3}c$

Figure 22: Effect of d_{max} on the ice shape

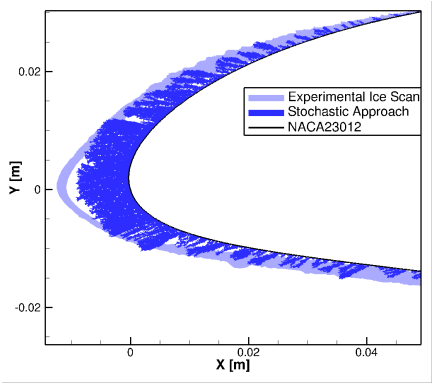

(a) $8.0 \times 10^{-3}c$

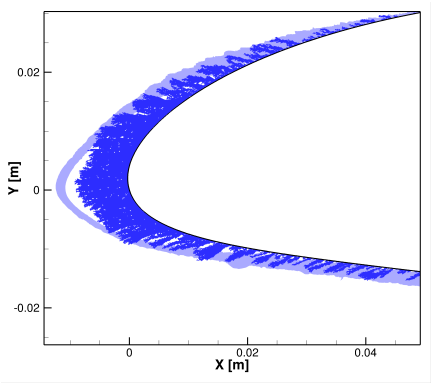

(b) $1.6 \times 10^{-2}c$

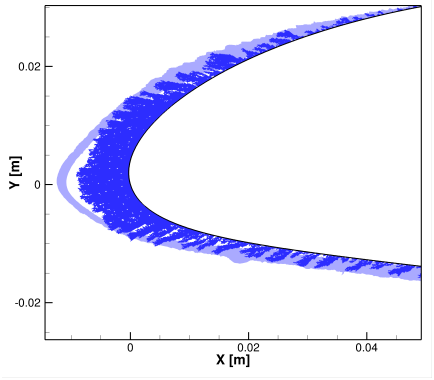

(c) $3.2 \times 10^{-2}c$

Figure 23: Effect of d_{max} on the ice shape (continued)

650 case-dependent, a limitation that will be addressed in future works.

Table 1: Test Cases Input Parameters

Case	Case 241 (Laurendeau et al., 2022)	Case 04 (Trontin et al., 2017)	Case 242 (Laurendeau et al., 2022)	Case 364 (Laurendeau et al., 2022)
Geometry	NACA23012	NACA0012	NACA23012	NACA0012
Chord [m]	0.4572	0.5334	0.4572	0.9144
Sweep [deg]	0.0	0.0	0.0	30.0
AoA [deg]	2.0	4.0	2.0	0.0
Mach [-]	0.32	0.32	0.31	0.35
Temperature [K]	250.70	262.3	265.65	259.60
Pressure [kPa]	92.528	101.325	92.941	89.632
LWC [g/m^3]	0.42	0.6	0.75	0.5
MVD[μm]	30.0	15.0	15.4	20.5
Icing Time [s]	300	384	300	1020
Roughness [μm]	457.2	533.4	457.2	914.4

The average numbers of ice elements generated for each test case are reported in table 2. The experimental droplet size distributions used for Cases 241, 242 and 364 are reported in table 3.

Table 2: Average numbers of ice elements generated for each test case

	Case 241	Case 04	Case 242	Case 364
$\bar{N}_{\text{ice,elem}}$	63286	49717	62196	59282

Table 3: Discrete Droplet Size Distributions

Case 241		Case 242		Case 364	
Dia. [μm]	Fraction LWC [-]	Bin [μm]	Fraction LWC [-]	Bin [μm]	Fraction LWC [-]
6.9	0.05	6.7	0.05	6.4	0.05
9.8	0.10	8.9	0.10	8.7	0.10
14.7	0.20	11.3	0.20	11.7	0.20
30.3	0.30	15.0	0.30	20.3	0.30
60.5	0.20	20.8	0.20	36.9	0.20
100.4	0.10	27.3	0.10	61.4	0.10
163.8	0.05	36.0	0.05	99.9	0.05

4.1. Case 241

The ice shape for Case 241 is computed using $\delta = 2.5 \times 10^{-4}c$ and $d_{max} = 2.0 \times 10^{-3}c$. The experimental droplet size distribution is used to obtain the impingement map (Laurendeau et al., 2022). The results of five trials, each using a different sequence of PRNs, are overlaid in Figure 24. Here, the air pockets within the ice are not pictured for clarity's sake. The likelihood of the ice shape is shown with the grayscale and is obtained by decreasing the opacity level of each result to 20%. Therefore, a darker area in Figure 24 corresponds to a zone it is more likely to observe ice. The experimental result presented in light blue in Figure 24 is obtained from a spanwise invariant geometry. The light blue zone thus corresponds to the projection of the experimental ice envelope along the entire span on the xy-plane.

The stochastic ice shapes are in good agreement with the experimental results: the ice thickness at the leading edge matches the expected range and the tapered shape of the experimental ice is well captured. The latter is missed by the 5-layers determinist result of CHAMPS, which has a rounded shape.

The zones of higher variability are mainly where feathers are observed numerically in Figure 24. This means that the feathers are formed at random locations downstream of the main ice accretion. It corresponds to the expected behavior, as the experimental ice envelope is thicker for the same zones and the ice scan shows discrete ice structures within these areas (Lee et al., 2014). This observation is highlighted in Figure 25, where the ice shape for a single trial is presented. One can also observe the agreement between the experimental ice limits and the stochastic result.

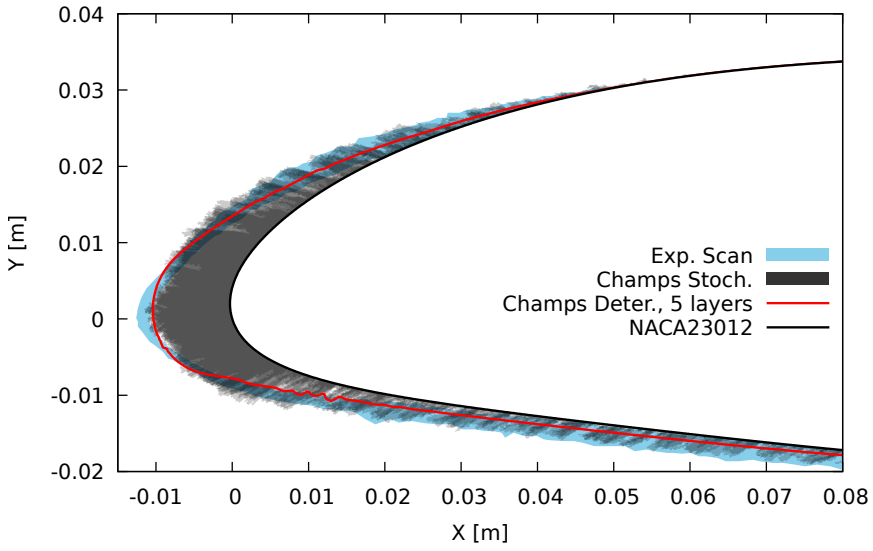

Figure 24: Results for Case 241

4.2. Case 04

Case 04, presented originally by Trontin et al. (2017), is a glaze ice case leading to the accretion of 2 ice horns. The stochastic ice shape is obtained for an element size of $\delta = 2.5 \times 10^{-4}c$ and for $d_{max} = 8.0 \times 10^{-3}c$, and a monodisperse droplet size distribution is used due to the unavailability of the experimental data. Again, the results for five trials are presented in Figure 26 and are compared to the deterministic results of CHAMPS for a single layer

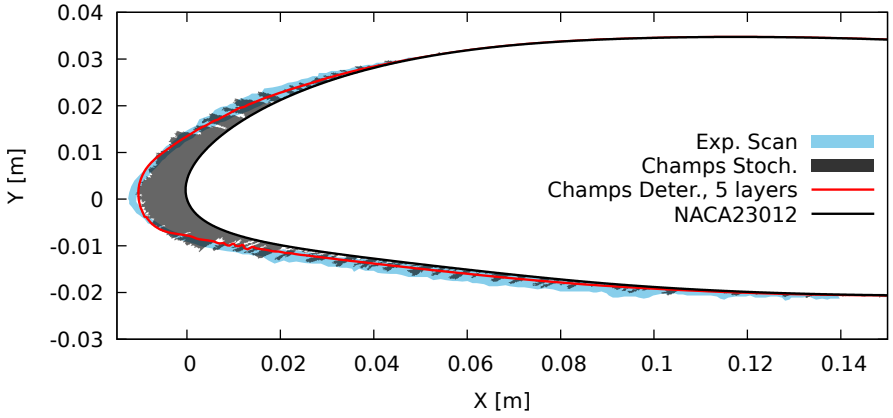

Figure 25: Result of one trial for Case 241

and of IGLOO2D using a predictor/corrector framework (Trontin et al., 2017).

The stochastic method successfully captures the upper ice horn, even if it corresponds to a single-layer framework. However, the lower horn is missed and there is a discrepancy in the ice thickness at the stagnation point. It suggests that runback water film on the lower surface is not well captured by the Iterative Messinger model for a single layer simulation. The same observation can be made for the determinist result of CHAMPS, supporting this assumption. Thus, for such ice geometries, an extension of the stochastic method to a multi-layer framework is required. A multi-layer framework would require the extraction of the highly irregular discrete ice front, followed by a post-treatment of the extracted front to obtain a meshable geometry. An approach similar to the one proposed by Bourgault-Côté (2019) could be used. The latter involves the conversion of the discrete ice front to a smooth B-Spline geometry, taking into account the morphology of the ice (i.e. concave and convex features) to provide an adequate discretization of the geometry. This method is used in a multi-layer stochastic ice accretion model based on a Cartesian advancing front technique also proposed by Bourgault-Côté (2019).

The ice shape obtained with IGLOO2D results from the imposition of an ice density computed with an empirical model based on the surface temperature.

Therefore, care must be taken when comparing the results of the predictor step of IGLOO2D to the stochastic ice shape, in which the ice density is a dependent variable.

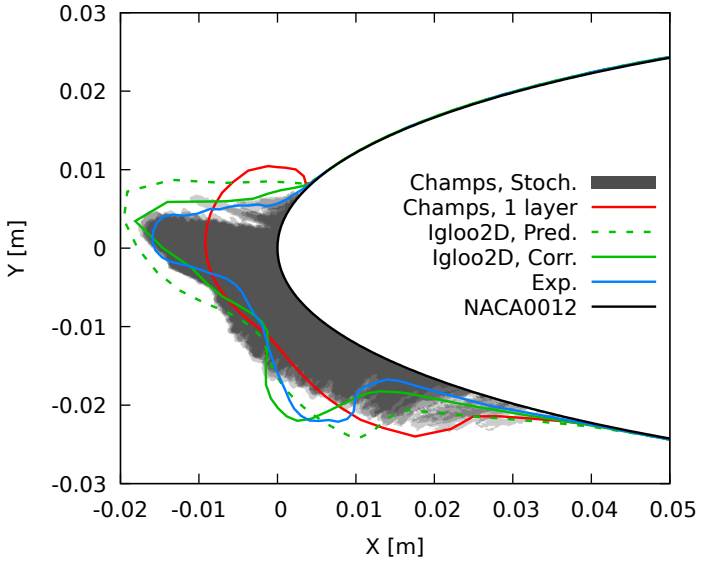

Figure 26: Results for Case 04

4.3. Case 242

The second glaze ice case selected for the model validation is Case 242 presented at the first IPW (Laurendeau et al., 2022). It features two ice horns and was one of the least successful cases presented at the IPW. The droplet size distribution is set to a monodisperse distribution. Figure 27 shows the results of the stochastic method (for $\delta = 2.5 \times 10^{-4}c$ and $d_{max} = 8.0 \times 10^{-3}c$) compared to five experimental trials. The latter are plotted using a light blue scale, representing their likelihood, as explained previously. These ice contours were obtained from five different runs. They correspond to the tracing of the experimental ice shape cuts, perpendicular to the leading edge, in the spanwise direction (Laurendeau et al., 2022). Here, the result of CHAMPS deterministic is not presented since the solver fails to predict an ice shape for this case.

Compared to the experimental envelope (Figure 27), the stochastic method succeeds to well capture the thickness at the leading edge, the ice limits, and the position and angle of the horns. However, it fails to predict their height as well as the variability observed in the overall shape of the horns. Indeed, in Figure 27, only one trial of the stochastic method is shown by the solid dark blue line since no significant variation is observed between different runs. Only the surface details on the ice front vary; the global ice shape (i.e., the position and angle of the horns, the ice thickness, and the ice limits) stays constant. It suggests that other sources of stochasticity are involved in the icing process and need to be modeled by the stochastic method to predict the observed variability in the ice shapes.

This result is compared to the ice shapes presented by the participants of the IPW for the same case (Laurendeau et al., 2022) in Figure 28. The software used by the participants implement deterministic and either multi-layer or predictor-corrector frameworks. While their results are scattered, there are two main characteristics of the computed ice shapes that stand out: i) the ice limits are further downstream than the experiments, and ii) the ice horns are not captured or not well predicted, both for their position and their height. Nevertheless, the proposed stochastic method successfully predicts these two features of the ice, while implementing only a single-layer framework. It suggests that the method succeeds to capture small details in the ice shape due to the accretion of single elements of ice at a time. The few elements of ice generated at the beginning of the icing time are significant enough to predict the shadow zone associated with the right ice limits. These small ice structures are assumed to be linked to time scales smaller than the typical time step used in the multi-layer frameworks, which can explain why the latter miss the experimental ice limits and the formations of the two ice horns.

4.4. Case 364

The studied geometry for Case 364 is a swept-wing ($\Lambda = 30$ degrees). The flow and droplet fields and the thermodynamic exchanges are obtained from the

2D geometry using a 2.5D approach. In this method, the 2D RANS equations coupled with a crossflow equation are solved; more details on this approach are available in (Bourgault-Côté et al., 2017; Lavoie et al., 2018). The stochastic method is then used in the presented 2D framework without any modification. It is worth noting that in a 2.5D deterministic framework, the implementation of the thermodynamic and the geometry evolution models are not modified either (Lavoie et al., 2018). An element size of $\delta = 2.5 \times 10^{-4}c$ is used and $d_{max} = 1.0 \times 10^{-3}c$. The impingement map is obtained using the experimental droplet size distribution (Laurendeau et al., 2022). The results for five trials are presented in Figure 29. While the ice thickness at the leading edge respects the experimental thickness, the horn-like structures are missed. This is assumed to be a result of the single-layer framework: runback water (i.e., glaze ice state) is missed by the Iterative Messinger model due to the very cold conditions. Although the experimental ice shape has a very weak spanwise structure, a periodic variability of the ice shape is observed experimentally. This variability is generally attributed in part to phenomena, not modeled here, of shadowing

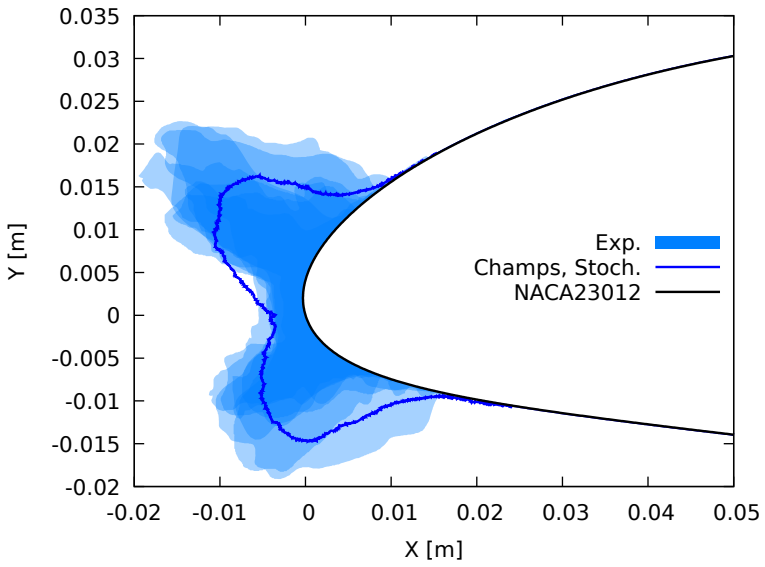

Figure 27: Results for Case 242

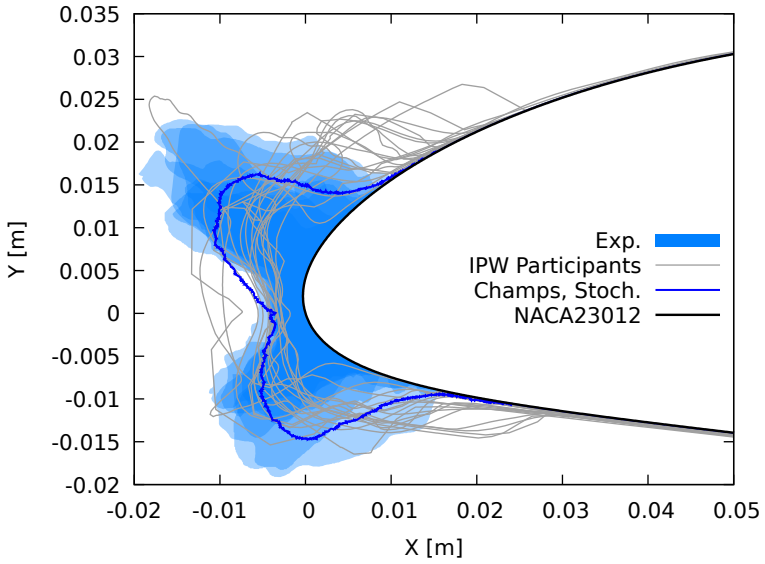

Figure 28: Results for Case 242 compared to the participants of the IPW (Laurendeau et al., 2022)

765 effects by the ice shape for the droplet trajectories along the spanwise direction. However, the model successfully captures the angle at which the main ice accretion grows, highlighted in Figure 30, where the result for a single trial is presented. Additionally, one can observe the geometry of the obtained ice feathers, appearing at discrete and random locations. Their prediction is in 770 agreement with the experimental ice scan for their position, height, and morphology. Such discrete ice structures are completely missed by the determinist result of CHAMPS. As for Case 241, the variability in the ice shape is mainly observed in the zone where feathers are formed.

5. Conclusion

775 An original ice accretion model is proposed to predict stochastic ice shapes as well as discrete morphologies such as ice feathers. It is developed in CHAMPS, a complete icing suite implementing a flow solver resolving the RANS equations,

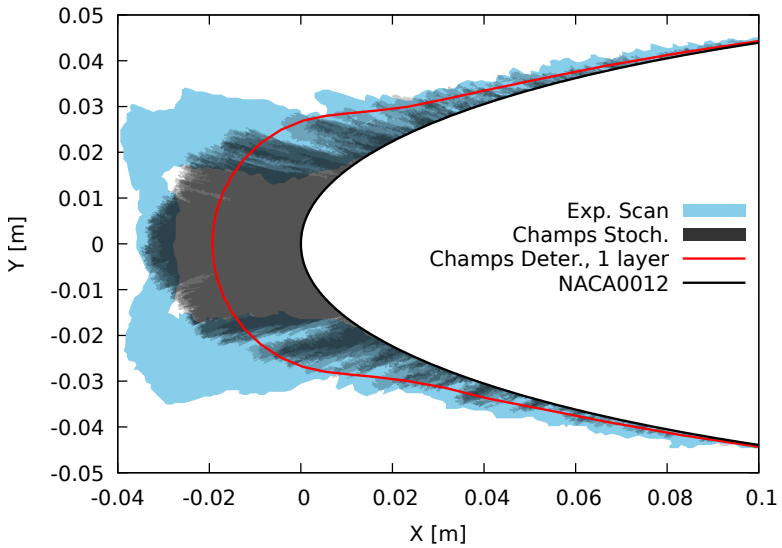

Figure 29: Results for Case 364

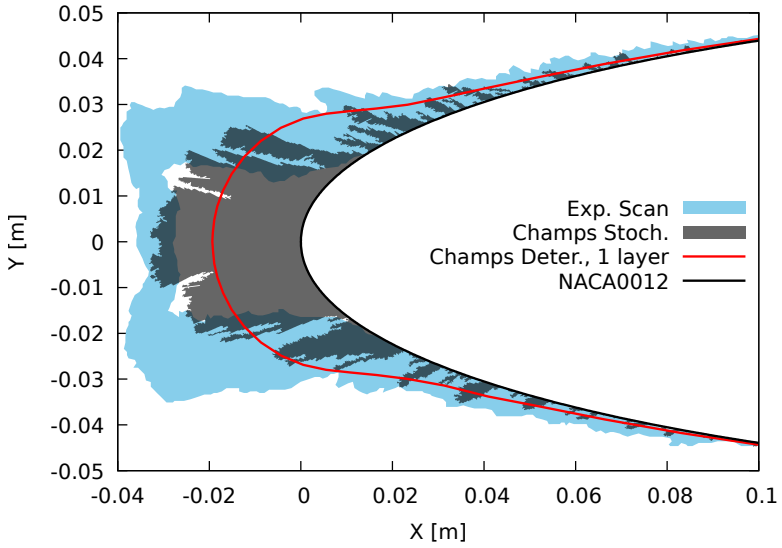

Figure 30: Result of one trial for Case 364

an Eulerian droplets impingement model, and an Iterative Messinger model for the thermodynamic exchange resolution.

The proposed baseline algorithm features an unstructured advancing front technique to model the ice accretion in a building block manner by successively accumulating single elements of fluid. The latter are seeded upstream of the studied geometry and their trajectories are extracted from the Eulerian droplet velocity field. Upon impingement, the thermodynamic state of a given fluid element, computed by the Iterative Messinger model, is checked to predict glaze ice conditions. The runback water is modeled by the motion of the fluid elements on the ice front. At each step of their motion, their thermodynamic state determines if it flows further downstream or if a new element of ice is generated. The verification of the impingement process is performed by comparing the collection efficiency obtained from the proposed stochastic method to the deterministic results for two cases of the literature. A space convergence study shows that the ice density converges as the element size decreases. The results of the baseline algorithm show that ice thickness is overestimated, suggesting the obtained ice density is too low. An extension of the developed 2D framework is thus proposed to model 3D mechanisms by introducing permeability in the front. Validation on four cases of the literature is performed. The resulting ice shapes are in good agreement with the experiments, both for rime and glaze conditions. The proposed method leads to the prediction of stochastic ice shapes and discrete ice structures. The method effectively captures the presence of feathers in the most downstream areas, especially in rime conditions. For glaze conditions, the presence of horns and the ice limits are better predicted than with deterministic quasi-steady approaches. This is attributed in particular to the unsteady growth process which allows modeling the shadowing effect.

The performances of the proposed method enable to envision future developments, such as extending the model to a multi-layer and 3D framework building on the experience of 3D literature (Szilder and Yuan, 2015) to improve the temporal and spatial accuracies. Finally, the investigation of other sources of stochasticity and their effects is required to accurately predict the randomness observed in experimental setups.

6. Acknowledgements

This work is supported by the National Sciences and Engineering Research Council of Canada (NSERC), the Fonds de Recherche du Québec Nature et technologies (FRQNT), the Canada Research Chair in Modelling and Control of Unsteady Aircraft Aerodynamics, and the Office national d'études et de recherches aérospatiales (ONERA). This research was enabled in part by support provided by Calcul Québec (www.calculquebec.ca) and Compute Canada (www.computecanada.ca). The authors would like to thank Dr. Simon Bourgault-Côté for the multiple enlightening discussions.

References

Blazek, J., 2015. Computational Fluid Dynamics: Principles and Application. 3^{rd} ed., Elsevier.

Bourgault, Y., Habashi, W.G., Dompierre, J., Baruzzi, G.S., 1999. A finite element method study of eulerian droplets impingement models. International Journal for Numerical Methods in Fluids 29, 429–449. doi:10.1002/(SICI)1097-0363(19990228)29:4<429::AID-FLD795>3.0.CO;2-F.

Bourgault-Côté, S., 2019. Ice Interface Evolution Modelling Algorithms for Aircraft Icing. Ph.D. thesis. Polytechnique Montreal. Montreal.

Bourgault-Côté, S., Ghasemi, S., Mosahebi, A., Laurendeau, E., 2017. Extension of a two-dimensional Navier-Stokes solver for infinite swept flow. AIAA Journal 55, 662–667. doi:10.2514/1.J055139.

Broeren, A., 2021. NASA Ice Shape Data for Case 242. URL: https://folk.ntnu.no/richahan/IPW/files/Presentations/IPW1_Presentations/Day%202/NASA%20Case%20242%20Data.pdf. 1st AIAA Ice Prediction Workshop.

Butnarasu, M., Habashi, W.G., Fossati, M., 2015. Optimization of the morphogenetic approach for in-flight icing, in: 53^{rd} AIAA Aerospace Sciences Meeting, AIAA Paper 2015-34, January. doi:10.2514/6.2015-0034.

Chan, W.M., 1999. Hyperbolic methods for surface and field grid generation, in: Thompson, J.F., Soni, B.K., Weatherill, N.P. (Eds.), Handbook of Grid Generation. 1^{st} ed.. CRC Press.

Chapel, 2022. The Chapel Programming Language. URL: https://chapel-lang.org/. last accessed: 2022-05-25.

Erhan, T., Murat, C., Serkan, O., 2011. Parallel computing applied to three-dimensional droplet trajectory simulation in lagrangian approach, in: SAE 2011 International Conference on Aircraft and Engine Icing and Ground Deicing, SAE International. URL: https://doi.org/10.4271/2011-38-0106, doi:https://doi.org/10.4271/2011-38-0106.

Forsyth, P., Szilder, K., 2022. Application of the Morphogenetic Approach to 1st AIAA Ice Prediction Workshop Test Cases, in: AIAA AVIATION 2022 Forum. URL: https://arc.aiaa.org/doi/abs/10.2514/6.2022-3609, doi:10.2514/6.2022-3609, arXiv:https://arc.aiaa.org/doi/pdf/10.2514/6.2022-3609.

Jin, H., Tanner, R.I., 1993. Generation of unstructured tetrahedral meshes by advancing front technique. International Journal for Numerical Methods in Engineering 36, 1805–1823. URL: https://onlinelibrary.wiley.com/doi/abs/10.1002/nme.1620361103, doi:https://doi.org/10.1002/nme.1620361103, arXiv:https://onlinelibrary.wiley.com/doi/pdf/10.1002/nme.1620361103.

Laurendeau, E., Bourgault-Cote, S., Ozcer, I.A., Hann, R., Radenac, E., Pueyo, A., 2022. Summary from the 1st AIAA Ice Prediction Workshop. doi:10.2514/6.2022-3398.

Lavoie, P., 2017. A Numerical Model Simulating Thin Water Films on Swept Wings in Icing Condition. Master's thesis. Polytechnique Montréal.

Lavoie, P., Bourgault-Côté, S., Laurendeau, E., 2018. Numerical algorithms for infinite swept wing ice accretion. Computers & Fluids 161, 189–198. doi:10.1016/j.compfluid.2017.11.015.

Lavoie, P., Laurendeau, E., Pena, D., Hoarau, Y., 2016. Comparison of thermodynamic models for ice accretion on airfoils. International Journal of Numerical Methods for Heat and Fluid Flow doi:10.1108/HFF-08-2016-0297.

Lee, S., Broeren, A.P., Kreeger, R.E., Potapczuk, M.G., Utt, L., 2014. Implementation and validation of 3-d ice accretion measurement methodology, in: 6th AIAA Atmospheric and Space Environments Conference. doi:10.2514/6.2014-2613.

Leroy, A., 2004. Étude expérimentale et numérique des dépôts de givre discontinus sur les voilures en flèche daéronefs. Ph.D. thesis. Université Blaise Pascal. Clermont-Ferrand.

Lohner, R., Parikh, P., 1988. Generation of three-dimensional unstructured grids by the advancing-front method. International Journal for Numerical Methods in Fluids 8, 1135–1149. doi:https://doi.org/10.1002/fld.1650081003.

Menter, F.R., 1992. Improved Two-Equation k-omega Turbulence Models for Aerodynamic Flows. Technical Report. NASA TM 103975.

O'Neill, M.E., 2014. PCG : A Family of Simple Fast Space-Efficient Statistically Good Algorithms for Random Number Generation. URL: https://www.cs.hmc.edu/tr/hmc-cs-2014-0905.pdf.

Oztekin, E., 2021. Analysis using LEWICE/3D coupled with OVERFLOW. URL: https://folk.ntnu.no/richahan/IPW/files/Presentations/IPW1_Presentations/Day%202/%c3%96ztekin_FAA_LEWICE.pdf. 1st AIAA Ice Prediction Workshop.

Papadakis, M., Wong, S.C., Rachman, A., Hung, K.E., Vu, G.T., Bidwell, C.S., 2007. Large and Small Droplet Impingement Data on Airfoils and Two Simulated Ice Shapes. Technical Report. NASA. URL: https://ntrs.nasa.gov/api/citations/20070034950/downloads/20070034950.pdf.

Papillon-Laroche, H., 2022. Stochastic Ice Accretion Model for Aircraft Icing. Master's thesis. Polytechnique Montreal. Montreal.

Papillon-Laroche, H., Bourgault-Côté, S., Laurendeau, E., 2021. Multi-layer stochastic ice accretion model for aircraft icing, in: AIAA AVIATION 2021 Forum. doi:10.2514/6.2021-2629.

Parenteau, M., Bourgault-Cote, S., Plante, F., Kayraklioglu, E., Laurendeau, E., 2021. Development of Parallel CFD Applications with the Chapel Programming Language, in: AIAA Scitech 2021 Forum. URL: https://arc.aiaa.org/doi/abs/10.2514/6.2021-0749, doi:10.2514/6.2021-0749, arXiv:https://arc.aiaa.org/doi/pdf/10.2514/6.2021-0749.

Peraire, J., Peir, J., Morgan, K., 1992. Adaptive remeshing for three-dimensional compressible flow computations. Journal of Computational Physics 103, 269–285. URL: https://www.sciencedirect.com/science/article/pii/002199919290401J, doi:https://doi.org/10.1016/0021-9991(92)90401-J.

Pointwise, I., 2022. Pointwise. URL: https://www.pointwise.com. last accessed: 2022-06-25.

Porter, C.E., 2022. A comparison of trajectory refinement schemes for glennice, in: AIAA AVIATION 2022 Forum. URL: https://arc.aiaa.org/doi/abs/10.2514/6.2022-3692, doi:10.2514/6.2022-3692, arXiv:https://arc.aiaa.org/doi/pdf/10.2514/6.2022-3692.

Press, W.H., Teukolsky, S.A., Vetterling, W.T., Flannery, B.P., 2007. Numerical Recipes - The Art of Scientific Computing. 3^{rd} ed., Cambridge University Press.

Rendall, T., Allen, C., 2014. Finite-volume droplet trajectories for icing simulation. International Journal of Multiphase Flow 58, 185–194. doi:10.1016/j.ijmultiphaseflow.2013.08.007.

Roe, P., 1981. Approximate riemann solvers, parameter vectors, and difference schemes. Journal of Computational Physics 43, 357–372. doi:10.1016/0021-9991(81)90128-5.

Shaw, R., Kostinski, A., Larsen, M., 2002. Towards quantifying droplet clustering in clouds. Quarterly Journal of the Royal Meteorological Society 128, 1043 – 1057. doi:10.1256/003590002320373193.

Spalart, P.R., Allmaras, S.R., 1992. A one-equation turbulence model for aerodynamic flows, in: 30^{th} Aerospace Sciences Meeting and Exhibit, AIAA Paper 1992-439. doi:10.2514/6.1992-439.

Sugiyama, M., 2016. Chapter 19 - Numerical Approximation of Predictive Distribution, in: Introduction to Statistical Machine Learning. Morgan Kaufmann, Boston, pp. 205–220. URL: https://www.sciencedirect.com/science/article/pii/B9780128021217000303, doi:https://doi.org/10.1016/B978-0-12-802121-7.00030-3.

Szilder, K., Lozowski, E.P., 2004. Novel two-dimensional modeling approach for aircraft icing. Journal of Aircraft 41, 854–861. doi:10.2514/1.470.

Szilder, K., Yuan, W., 2015. The influence of ice accretion on the aerodynamic performance of a UAS airfoil, in: 53^{rd} AIAA Aerospace Sciences Meeting, AIAA Paper 2015-536. doi:10.2514/6.2015-0536.

Trontin, P., Blanchard, G., Kontogiannis, A., Villedieu, P., 2017. Description and assessment of the new ONERA 2D icing suite IGLOO2D, in: 9^{th} AIAA Atmospheric and Space Environments Conference, AIAA Paper 2017-3417. doi:10.2514/6.2017-3417.

Trontin, P., Villedieu, P., 2018. A comprehensive accretion model for glaciated icing conditions. International Journal of Multiphase Flow 108, 105–123. doi:https://doi.org/10.1016/j.ijmultiphaseflow.2018.06.023.

Yuki, K., Yamamoto, M., 2014. SLD Icing Simulation on NACA Airfoil Using MPS Method, in: The Proceedings of The Computational Mechanics Conference, The Japan Society of Mechanical Engineers. doi:10.1299/jsmecmd.2014.27.693.

Zhu, C., Fu, B., Sun, Z., Zhu, C., 2012. 3D Ice Accretion Simulation for Complex Configuration basing on Improved Messinger Model, in: International Journal of Modern Physics: Conference Series, World Scientific. pp. 341–350. doi:10.1142/S2010194512008938.

Highlights

- Stochasticity in the modeling of in-flight ice accretion is often neglected in icing software.
- Variability observed in experimental ice shapes is therefore not modeled.
- The ice accretion modeling in a building block manner enables the introduction of stochasticity.
- Introduction of stochasticity in the impingement allows to model stochastic ice shapes.

Author statement:

Hélène Papillon Laroche: Conceptualization, Methodology, Software, Validation, Formal analysis, Visualization, Writing - Original Draft, Writing- Reviewing and Editing
Emmanuel Radenac: Conceptualization , Supervision, Writing- Reviewing and Editing
Éric Laurendeau: Conceptualization , Supervision, Writing- Reviewing and Editing

Declaration of interests

☒ The authors declare that they have no known competing financial interests or personal relationships that could have appeared to influence the work reported in this paper.

☐ The authors declare the following financial interests/personal relationships which may be considered as potential competing interests: